A New Interpretation of Hot Gas Ingress Through Turbine Rim Seals Influenced by Mainstream Annulus Swirl

Dimitrios Graikos, Hui Tang, Carl M Sangan, Gary D Lock and James A Scobie
dg698@bath.ac.uk, h.tang2@bath.ac.uk, c.m.sangan@bath.ac.uk, g.d.lock@bath.ac.uk and j.a.scobie@bath.ac.uk
Department of Mechanical Engineering
University of Bath
Bath, BA2 7AY
United Kingdom

ABSTRACT

Rim seals are fitted at the periphery of the stator and rotor discs to reduce the adverse effects of hot gas ingress on highly stressed turbine components limited by temperature. Ingress is induced by rotational effects such as disc pumping, as well as by asymmetric pressure-driven unsteady phenomena. These influences superpose to form a complex flow-physics problem that is a challenge for computational fluid dynamics. Engine designers typically use practical low-order models that require empirical validation and correlating parameters. This paper identifies the swirl ratio in the mainstream annulus as a dominant characterising parameter to predict ingress. This is a new interpretation that is supported by extending a low-order model based on turbulent transport using an effective eddy mixing length based on the difference in swirl between the annulus and seal clearance.

Experimental measurements were made using a 1.5-stage turbine rig at low Reynolds number. The influence of annulus swirl ratio was investigated over a range of flow conditions and two rim-seal geometries, with the ingress quantified using CO_2 tracer concentration in the sealing flow. The concentration data were complemented by measurements in the annulus using a five-hole aerodynamic probe.

1 INTRODUCTION

Ultra-high efficiency for turbomachinery components is important in the acceleration of technology to net zero emissions for flight and land-based power. Secondary Air Systems play a critical role in limiting the metal temperatures (and hence stresses) in engines, but inherently generate a thermodynamic loss in the primary power cycle and aerodynamic losses in the turbine. Air is diverted from the compressor to provide internal and film cooling, to dissipate heating from windage, and to act as purge that supresses ingress (or ingestion) of hot gases into the turbine cavities formed between stator assemblies and rotating discs. Rim-seals are fitted at the periphery of these cavities to reduce the purge required to maintain the temperatures of discs to an acceptable level.

The physical mechanisms governing ingress are multifaceted: these include fluid interactions between the rim-seal, vane and blade; rotational effects of disc pumping and purge; shear-layer instabilities and rotating modes; and turbulent mixing over a range of length scales. Predicting the performance of rim-seals is a challenge for computational fluid dynamics and successful application of numerical simulation as a practical design tool is limited. Engine designers typically rely on expedient low-order models, validated empirically using turbine rigs operating with tracer gases as a proxy for cavity temperature; such rigs generally simulate the engine environment but usually at low Reynolds number and pressure ratio. The designer would wish for a model with genuinely predictive capability at engine-operating conditions, rather than one that were rig specific or required experimental characterisation.

In this paper experiments were conducted in a 1.5-stage turbine rig using two rim-seals in a cavity downstream of the rotor, where the swirl in the annulus was varied (positively or negatively) by controlling the flow coefficient. The analysis presents a new interpretation of the fluid dynamics governing ingress, which is supported by

extending a low-order model based on turbulent transport. An effective turbulent diffusivity (proportional to a representative mixing length) is used to subsume all transportation mechanisms, including pressure variations in the annulus and effects of shear between the annulus and the seal clearance flows. Based on experimental observation, this mixing length is modelled principally as a function of the difference in swirl between the annulus and rim-seal clearance; larger differences in swirl lead to stronger effects of shear and in turn amplified diffusion and increased flux of ingress.

The results are of practical interest to the engine designer providing improved predictive capability for thermal management, especially in terms of scaling rig data to engine conditions.

2 LITERATURE REVIEW

Figure 1 illustrates a typical turbine stage with cavities (or wheel-spaces) upstream and downstream of the rotor. The velocity triangles at the hub show flow components and angles in the absolute $(C, \alpha)_{2,3}$ and rotating $(V, \beta)_{2,3}$ frames of reference. The stage may be characterised by an annulus flow coefficient or Rossby number $C_F = W/\Omega r$ based on the ratio of the axial velocity of the flow to the rotational speed of the disc.

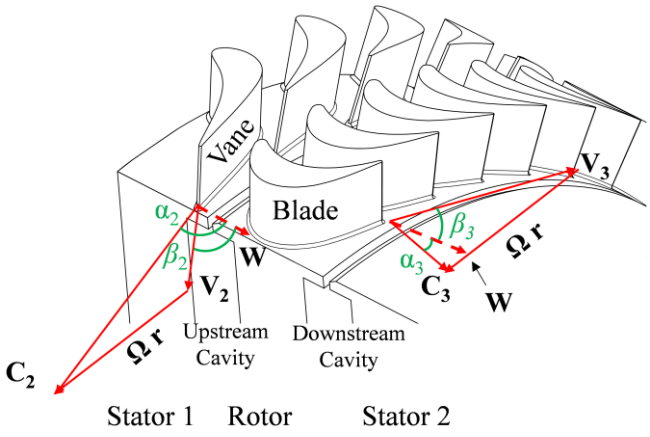

Figure 1: Turbine stage showing upstream and downstream velocity triangles

Chew *et al.* [1] recently reviewed the scientific literature related to ingress, describing three primary (but connected) fluid-dynamic mechanisms. *Rotationally-driven* effects occur when the purge and recirculation of ingested flow in the cavity form a boundary layer pumped by the disc. *Pressure-driven* effects originate in the annulus flow, with high swirl and non-axisymmetric characteristics created by stationary vanes and rotating blades. *Intrinsically unsteady* effects related to interaction between the purge and annulus flows are manifested as large-scale structures rotating below the blade-passing frequency, though their significance relative to vane and blade pressure asymmetries is not clear.

Despite the complexity of the flow physics, experimental data collected on turbine rigs have been successfully interpreted by elementary, low-order models. Owen [2][3] produced orifice models based on pressure differences for rotationally-induced (RI) and externally-induced (EI) ingress, forming equations of a similar characteristic that relate the rim-seal effectiveness to a non-dimensional sealing-flow rate. These equations show that EI ingress generally dominates over rotational effects for rim-seals in proximity to the annulus. It is difficult to separate experimentally the influence of EI and RI drivers, and combined modes of ingress are important for double or multiple seals that extend to lower radii in the cavity.

The orifice model equations quantify the minimum sealing flow rate to prevent ingress and require empirical discharge coefficients that depend on seal geometry. Calibration of similar models against experimental data has been described by Johnson *et al.* [4], who introduced different discharge coefficients for ingress and egress. Ingress occurs for flow rates less than the sealing minimum, with a sealing effectiveness usually determined in experimental rigs using purge with a tracer concentration modified to

differ from that in the external flow. Scobie *et al.* [5] used the Owen models to determine empirical constants to successfully correlate and collapse data with variable external pressure asymmetry from a wide range of sources in the literature.

An ingress model based on turbulent transport through the rim seal was presented by Graber *et al.* [6] and further developed by Savov and Atkins [7] to broadly capture the full extent of available published experimental data. At the heart of the model is the mixing-length hypothesis for eddy diffusivity introduced by Prandtl [8]. Here the turbulent process is interpreted as the chaotic transport of fluid packets over a defined mixing-length scale from a region of one velocity to another region of a different velocity. The mixing length is an empirical parameter in the model but associated with the physical dimensions of the rim seal. The dominant source of mixing is assumed to be driven by recirculating flow in the rim-seal. The interaction between the mainstream and purge creates a toroidal vortex in a gap recirculation zone (GRZ), as first postulated by Ko and Rhode [9]. Savov and Atkins used a modulated diffusivity to account for the changing size, relative volume fraction and shape of the GRZ under different levels of momentum flux between purge and mainstream. With reference to Figure 1, this relative momentum will depend on the annulus swirl and flow coefficient. The modulation of the GRZ at low, medium and high purge is illustrated in Figure 2; the GRZ diminishes as the purge is increased and is eventually ejected at high flow rates.

The turbulent transport model can also theoretically accommodate the purge to annulus density ratio, which is usually not engine representative in test rigs.

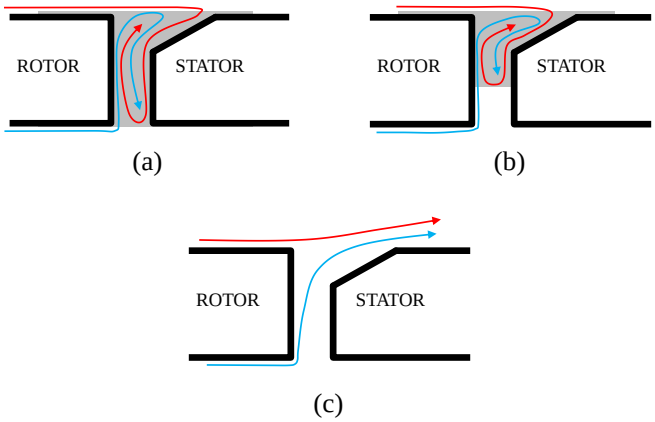

Figure 2: Hypothesised schematic illustrating the effect of purge on the GRZ at (a) low purge, (b) medium purge, (c) high purge - adapted from [7].

The orifice models and those based on turbulent transport can characterise effects of both rotation and external pressure fields. They cannot predict the unsteady influences created by large-scale structures in or near the rim seal. Pressure-modulated rotating flow modes have been computed by many studies, including Rabs *et al.* [10] who attributed their origin to shear-driven Kelvin-Helmholz phenomena. These have been identified by experiment (*e.g.* Beard *et al.* [11]) with fluid-dynamic features measured at frequencies unrelated to the vane and blade count, including pure RI conditions in the absence of external flow. These low-order models also only predict a monotonic relationship between effectiveness and purge flow. Graikos *et al.* [12] have shown that ingress is influenced by the interaction between the emergent purge from the rim seal and the impingement on downstream vanes and blades.

As discussed above, models are generally calibrated in turbine rigs and support practical design methodology; however, they are not truly predictive, nor do they confidently scale reliably to engine conditions at higher Mach and Reynolds numbers.

Currently there is no all-encompassing low-order model to accurately predict ingress for a general viscous turbulent flow.

Previous studies (*e.g.* [3-5], [13-14] and others) have attributed the circumferential pressure asymmetries in the annulus as the driving mechanism for ingress. It was shown that as the annulus flow coefficient C_F increased, the annulus pressure asymmetries (quantified by the peak-to-trough non-dimensional pressure variation, $\Delta C_{p,a}$) increased, and the ingress was generally enhanced. However, for a set vane angle the increase in swirl ratio and C_F is not decoupled. Further, it was shown there was a critical C_F where the ingress reached a minimum, which was inconsistent with the increased $\Delta C_{p,a}$. This paper presents a new interpretation that departs from the traditional theory. Instead of correlating with non-axisymmetric pressure variations, ingress is shown to even occur under axisymmetric pressure conditions and can be correlated to the swirl ratio in the annulus.

3 EXPERIMENTAL FACILITY

The 1.5-stage axial turbine rig at the University of Bath [15] has been used to experimentally measure ingress in the aft wheel-space (*i.e.,* downstream of the rotor disc). The rig operated under fluid dynamically scaled conditions at rotational Reynolds number 10^6 and vane exit Mach number up to 0.45. The facility was designed to accommodate modular bladed discs (bliscs) and bladed rings (with vanes) for expedient testing of rim-seals.

A cross-section of the rig is shown in Figure 3. Compressed air was supplied to the mainstream annulus through a 160 kW Atlas Copco ZS variable speed screw blower capable of delivering flow up to 1.5 kg/s at a pressure of 1.2 bar gauge. The flow was regulated by altering the load to the compressor and measured using a thermal mass

flow meter. A heat exchanger ensured that the air temperature was 20 $\pm$ 2˚C. An upstream radial diffuser was used to create axisymmetric flow at entry to the test section featuring 32 vanes. Rotors with different degrees of reaction, Λ, were machined as bliscs from a single piece of titanium, each with 48 turned blades. All the aerodynamic profiles (vanes and blades) were prismatic (2D) and designed by Siemens. The outer diameter of the rotors were 439 mm; the bliscs were rotated up to 6000 rpm by a 34 kW dynamometer, which could also absorb any power generated by the blades. Torque was measured using an HBM T12 torque transducer installed in the drivetrain. A vaneless stator platform was installed downstream of the rotor for all configurations used in this study.

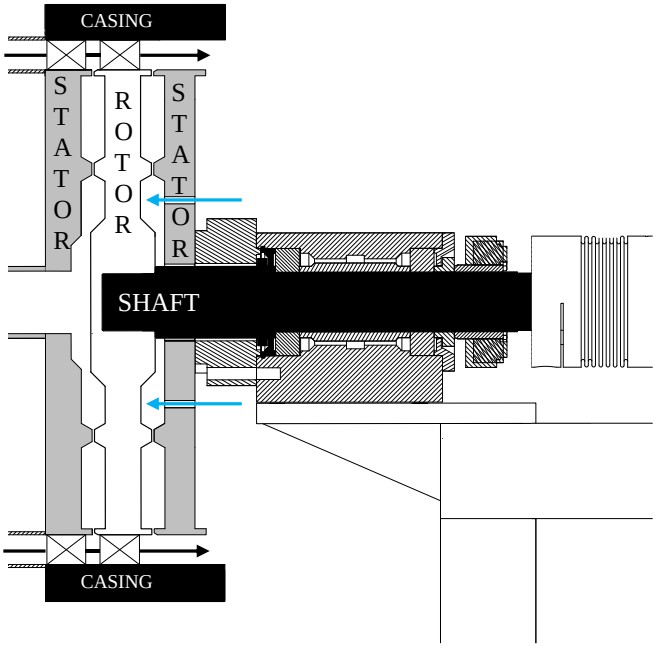

Figure 3: Cross-section of rig – blue arrows indicate sealing flow to the downstream wheel-space. Mainstream flow from left-to-right

Sealing flow was introduced to the downstream wheel-space at a low radius inboard of an inlet seal, ensuring the purge entering the outer wheel-space was axisymmetric and well-conditioned. Depending on the purge level supplied, one of three Bronkhorst

thermal mass flow controllers (accuracy of ±1% of full-scale range) were used to regulate and measure the flow rate. The sealing flow rate is expressed in non-dimensional form as Φ_0, equivalent to the ratio of the mean radial flow velocity through the seal to the disc speed. This has been shown to be a useful correlating parameter for both RI and EI ingress in the orifice and turbulent transport models [2,3,7].

$$\Phi_0 \equiv \frac{C_{w,0}}{2\pi G_c Re_\phi} = \frac{U}{\Omega\, b} \tag{1}$$

All symbols are defined in the nomenclature.

3.1 Operating Conditions

The operating conditions for the rig are summarised in Table 1. A range of flow coefficient, C_F (evaluated at $r = b$) was achieved by keeping the rotor speed constant and varying the annulus mass flow rate.

Parameters	**Disc Speed (rpm)**
	3000
Rotational Reynolds Number, Re_ϕ	7.4×10^5
Axial Reynolds Number, Re_w	$(0.7 – 4.4) \times 10^5$
Flow Coefficient, C_F	0.1 – 0.6
Vane exit Mach Number, M	0.08 – 0.45
LR Blade exit Mach Number, M	0.02 – 0.13
HR Blade exit Mach Number, M	0.03 – 0.17
Pressure ratio across full stage	1.01 – 1.35

Table 1: Operating conditions (see Nomenclature)

3.2 Gas Concentration Measurements

Levels of ingress from the annulus to the wheel-space were measured using a gas concentration technique. The sealing flow was seeded with a tracer gas: 0.5 – 1% CO_2. The sealing effectiveness (ε_c) is defined as follows:

$$\varepsilon_c = \frac{c - c_a}{c_0 - c_a} \tag{2}$$

Here c is the measured concentration and the subscripts a and 0 denote the values measured in the annulus and in the sealing flow at the inlet to the wheel-space respectively. The annulus flow had an inherent concentration, $c_a \approx 0.045\%$ - equivalent to atmospheric levels of CO_2 in air.

The concentration of CO_2 was measured using a Signal Group 9000MGA multi-gas analyser coupled to a 20-channel multiplexer. The multiplexer consisted of solenoid valves that were triggered to sample flow from up to 20 different locations in series. The radial distribution of concentration taps on the stator surface in the wheel-space downstream of the rotor is shown in Figure 4. The gas analyser had an accuracy, repeatability and linearity of $\pm 0.5\%$ of its full-scale range. The gas sampled was analysed for at least 30 s before its concentration stabilised and was then subsequently averaged over 10 s.

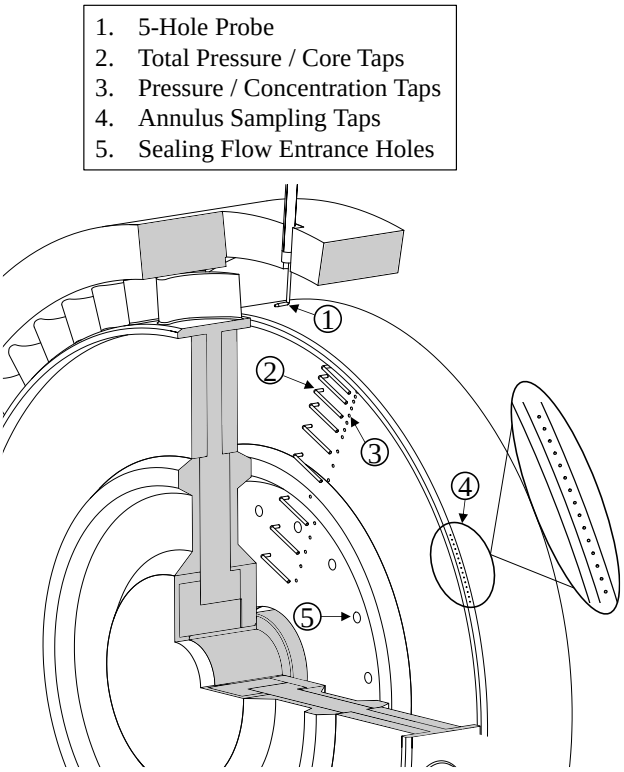

Figure 4: Downstream annulus and wheel-space test section and instrumentation.

3.3 Wheel-Space Swirl Velocity Measurements

Four Scani-valves, each with 48 channels, allowed pressures to be measured using a single differential transducer, reducing measurement uncertainty. Pressure was sampled and averaged over 2 s at each measurement location.

Static pressure was collected in the wheel-space from the same radial distribution of taps used for the concentration measurements. The tangential component of velocity in the wheel-space, and hence the swirl inside the inviscid core, was determined from total pressure measured at $z/S = 0.25$ using pitot probes – see Figure 4.

An *L-shaped* five-hole aerodynamic probe (Vectoflow) was installed through the outer casing of the rig to acquire measurements of velocity in the turbine annulus. The head diameter of the probe was 1.6 mm. The probe was traversed radially across the annulus height, h = 25 mm, at a fixed angular position using an in-house traversing

tower. The probe was used to measure the axial (W) and tangential (C_ϕ) components of velocity, from which the resultant absolute velocity (C) was deduced. Knowledge of the disc speed then allows for a calculation of the relative velocity (V) – see Figure 5.

3.4 Rotor designs

The turbine rig was specifically designed to accommodate modular bliscs for practical testing of rim-seals. Three interchangeable bliscs were used: two with turned rotor blades but of different degrees of reaction, and one with no blades (*i.e.* a rotating ring). The low- and high-reaction designs were used respectively by Patinios *et al.* [15] and Graikos *et al.* [12]. Note *high* and *low* are used to describe these rotors despite $0.3 < \Lambda < 0.47$ not being considered a high degree of reaction in terms of turbomachinery. The bliscs were driven off-design by the dynamometer at a fixed speed.

Parameter	Low Reaction	High Reaction
Blade Loading Coefficient (ψ)	2.95	3.65
Degree of Reaction (Λ)	0.30	0.47
Vane Exit Angle (α_2)	75.5°	75.5°
Relative Blade Inlet Angle (β_2)	49.7°	49.7°
Relative Blade Exit Angle (β_3)	70.2°	75°
Blade Exit Angle (α_3)	5.4°	46.1°
Blade Velocity Ratio (V_3/V_2)	1.9	2.5

Table 2: Rotor non-dimensional parameters at C_F = 0.407 evaluated at mid-span (r/b = 1.09)

Figure 5 shows the velocity triangles for the turbine stage. The angles and other characteristic features are quantified in Table 2 for the two rotors. The downstream velocity triangle is shown in more detail in Figure 5 (b), including the flow components and angles in the absolute (C_3, α_3) and rotating (V_3, β_3) frames of reference. The flow coefficient (C_F) and annulus swirl ratio (β) are defined below:

$$C_F = \frac{W}{\Omega r} \qquad (3)$$

$$\beta = \frac{C_{\phi 3}}{\Omega r} \qquad (4)$$

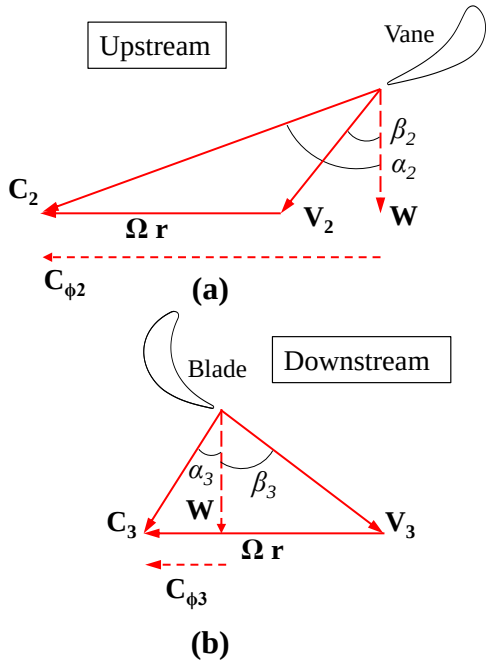

Figure 5: Detailed view of the (a) upstream and (b) downstream velocity triangles for a fixed flow-coefficient.

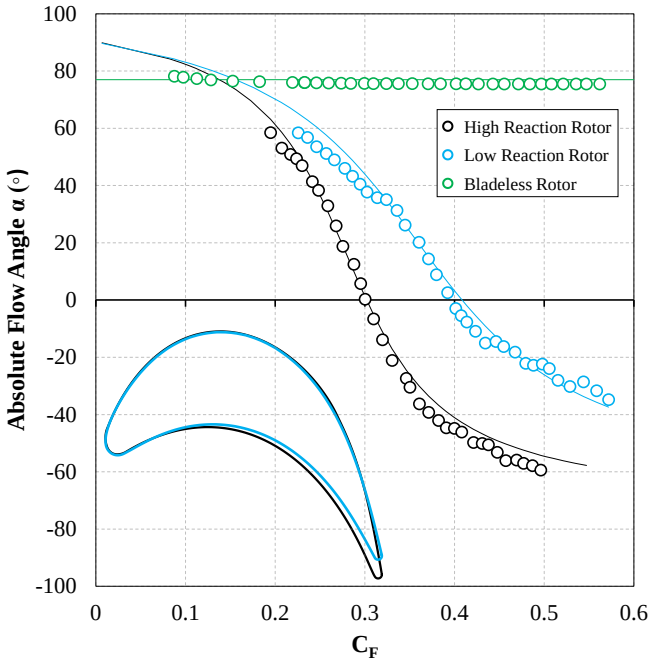

Figure 6: Variation of measured flow angle with flow coefficient downstream of the rotor. Lines represent isentropic theory.

Figure 6 shows the absolute flow angle α_3 measured by the probe at the mid-span of the annulus (at the axial position of the seal clearance) downstream of the rotor. These were obtained using the low- and high-reaction rotors, and the bladeless rotor (where $\alpha_3 = \alpha_2$ are essentially equal). The data was collected over the full range of C_F and agree well with the theoretical angles calculated from isentropic flow. As expected, there is a higher degree of turning and larger swirl opposing the rotor with increased reaction. The measured torque and power generated by the three configurations are shown in Figure 7. There is increased power generated as C_F (and the mass flow through the turbine) increases, and for the higher degree of reaction. The negative torque for the bladeless case quantifies the power required to drive the mechanical system, including frictional losses in the bearings and windage.

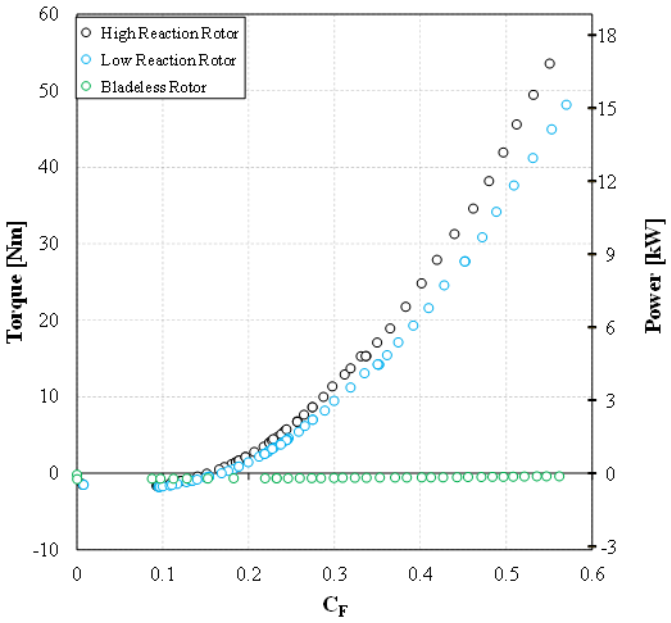

Figure 7: Torque and power measured against flow coefficient C_F for the three rotor configurations

3.5 Axial- and Double Radial-Clearance Seal Geometries

Generic axial- and double radial-clearance seals were used in the wheel-space downstream of the rotor. Figure 8 and Table 3 show the main characteristics of the seal geometry, that include a third-depth chamfer on the leading-edge of the stator platform. The double seal divides the wheel-space into outer and inner cavities. EI ingress is expected to dominate in the former and combined (both EI and RI) ingress in the latter.

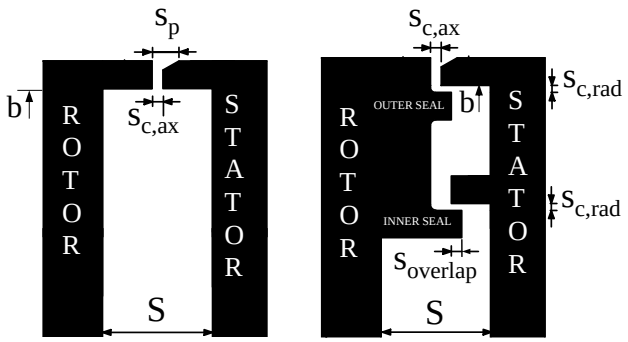

Figure 8: Axial- and Double Radial-Clearance Seals

The turbulent mixing length l_m contains an empirical parameter associated with the physical dimensions of the rim seal [7]. As shown in Section 4.2, l_m has been modelled as a function of the swirl ratio in the annulus. Figure 9 illustrates the axial-clearance in position downstream of the rotor for the three interchangeable configurations: bladeless, low- and high-reaction rotors. The annulus swirl above the rim seal was changed by varying the flow coefficient and by using the different geometric configurations. The experiments thus correlate the rim-seal effectiveness measured by gas concentration at r/b = 0.958 on the stator (see circle in Figure 9) in a manner where C_F and β are decoupled.

Parameter	**Dimension (mm)**
h	25
b	190
S	20
$s_{c,ax}$	2
$s_{c,rad}$	1.28
$s_{overlap}$	1.86

Table 3: Geometric parameters

4 RESULTS

Measurements of effectiveness were conducted in the downstream wheel-space with a vaneless stator installed downstream of the rotor. The superposition effect on sealing effectiveness of a downstream vane row, and the varied influence with C_F, was described in detail by Graikos *et al.* [12] and does not feature in this study. A downstream vane will affect the annulus swirl at flow coefficients that correspond to a

sweep (or arc) of absolute flow angle equivalent to an impingement on the leading edge of the downstream vane. Graikos *et al.* showed that ingress increased over a narrow range of C_F with the downstream vanes in position.

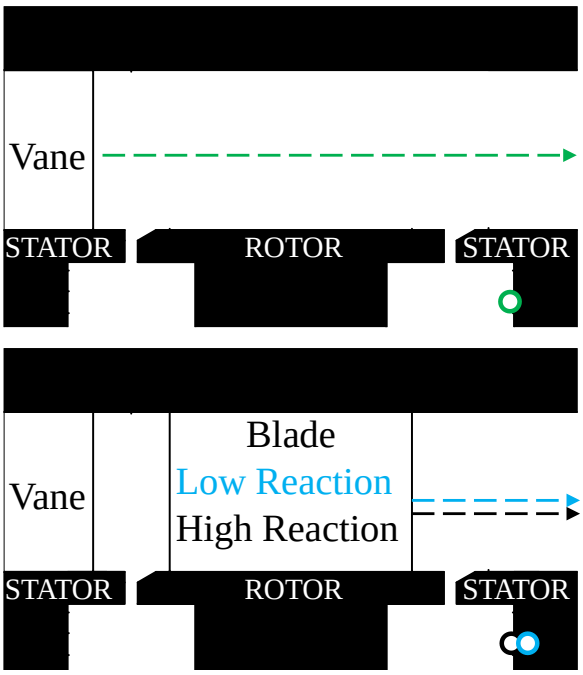

Figure 9: Downstream wheel-space measurement locations for the axial-clearance seal

4.1 Axial-clearance seal

In this section, experimental data is presented for a simple axial-clearance rim seal installed downstream of rotor disc. Effectiveness measurements were acquired in the downstream wheel-space at r/b = 0.958, as marked in Figure 9. This measurement position is considered representative for the wheel-space as previous publications [12] using this seal have shown only a minor variation in the radial distribution of effectiveness on the stator and rotating core.

Figure 10 shows the variation of concentration effectiveness (ε_c) in the downstream wheel-space against flow coefficient (C_F) for a fixed sealing flow rate (Φ_0). The data

were collected at constant rotational speed with the flow rate in the annulus varied to generate a range of C_F.

The high- and low-reaction blades feature a similar qualitative behaviour: a monotonic rise with increasing C_F to a peak in effectiveness, followed by a monotonic decrease. This effect is further interpreted in terms of the annulus swirl ratio below. The peak effectiveness for the low-reaction rotor is greater than that at higher reaction and the peak is shifted to higher C_F.

The characteristics are different for the case with no rotor blades. In the presence of mainstream flow ($C_F > 0$) the effectiveness reduces monotonically with increasing flow coefficient, falling steeply for $0.1 < C_F < 0.2$ before approaching a near-constant value where, as shown below, the annulus swirl ratio $\beta > 1$. In the absence of mainstream flow ($C_F = 0$), the rim-seal experiences RI ingress and here the effectiveness $\varepsilon_c \approx 0.63$. For most of the flow coefficient range ($C_F > 0.1$) the configuration for the rotor *without* blades results in the highest amount of ingress at high swirl. This is despite the rim seal being located significantly downstream from the vane, at an axial location where any associated non-axisymmetric circumferential pressure variation will have decayed to insignificance. The rotors with blades introduce an asymmetry near the rim seal in the rotating frame of reference; of greater significance is that they significantly reduce the swirl in the annulus.

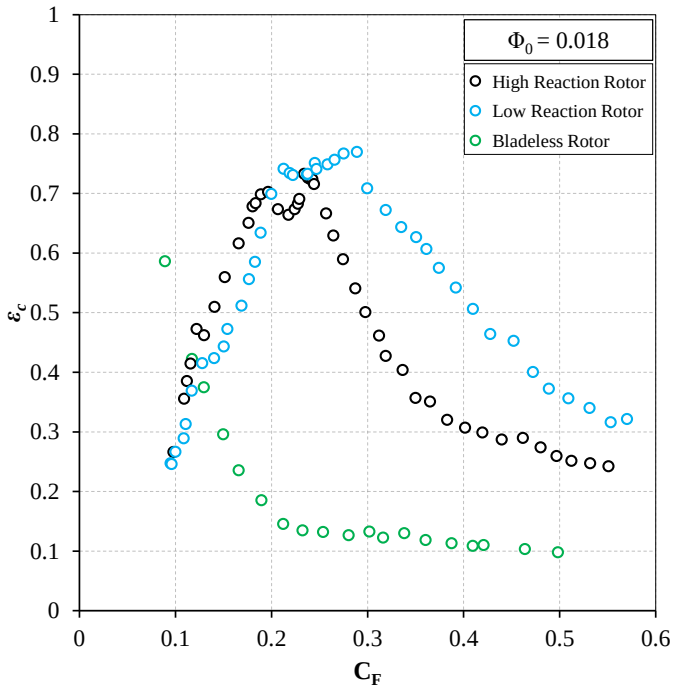

Figure 10: Variation of effectiveness against flow coefficient at *r/b* = 0.958 for the axial-clearance seal. (Green: Bladeless rotor, Black: High reaction rotor, Blue: Low reaction rotor) Φ_0 = 0.018.

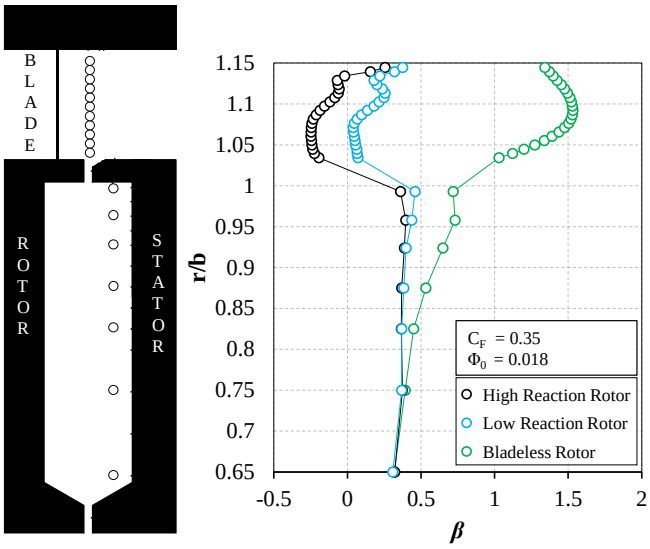

Figure 11: Radial distribution of swirl ratio β in the wheel-space and annulus for C_F = 0.35 and Φ_0 = 0.018. (Green: Bladeless rotor, Black: High reaction rotor, Blue: Low reaction rotor)

Figure 11 shows the radial distribution of swirl ratio in the downstream wheel-space and annulus for a fixed sealing flow rate and flow coefficient. Results for the three rotor configurations are presented. Positive values of β indicate that the tangential component of velocity acts in the direction of the disc rotation, while negative values indicate that the vectors are in opposition. Swirl ratios in the wheel-space were determined from measurements of static pressure on the stator wall and total pressure from the pitot tubes (at $z/S = 0.25$) shown in Figure 4. The measurements in the mainstream annulus were obtained from the five-hole aerodynamic probe. The ordinate (r/b) is geometrically aligned with the silhouette of the rig.

Consider the annulus swirl associated with the two bladed rotors. The swirl ratio is broadly invariant with radius for $r/b < 1.08$, beyond which is observed the radial migration of the secondary flow features and the tip leakage across the blades. The passage vortex creates an inflection in the swirl profile at $r/b > 1.1$. Consider the rotating platform without blades. In contrast to above, the swirl ratio increased with radius for $r/b < 1.08$ and the value at midspan is unlikely be representative of that ingested into the wheel-space near the hub.

The swirl ratio at the entry to the wheel-space at $r/b = 0.65$ is consistent for all three configurations ($\beta \approx 0.3$) and is invariant with C_F. The entry swirl depends on the sealing flow rate, with the core rotation reducing as Φ_0 increases. For the bladeless case, the swirl ratio increased radially due to ingress at high positive swirl from the annulus. While less pronounced, there is also an influence of annulus swirl at the periphery of the wheel-space for the two bladed rotors.

The measurements show a significant change in swirl across the rim seal dividing the wheel-space and annulus; this is associated with the gradient in shear stress hypothesised to promote the large-scale structures (or unsteady flow modes) observed

in the literature. Measurements at other flow coefficients showed qualitatively similar trends.

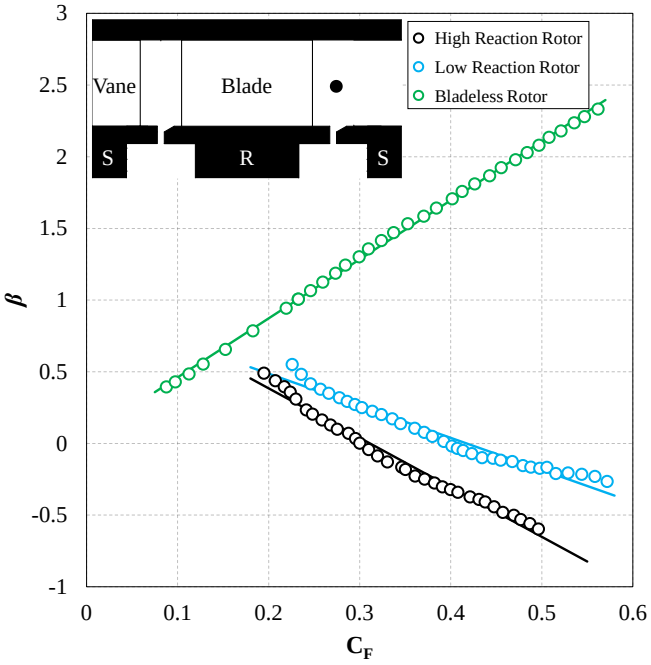

Figure 12: Variation of swirl ratio at the annulus mid-span β against flow coefficient C_F. (Green: Bladeless rotor, Black: High reaction rotor, Blue: Low reaction rotor)

Figure 12 (which can be compared with Figure 6 and associated velocity triangles) shows the variation of the swirl ratio (β) in the annulus against flow coefficient (C_F) measured at mid-span (r/b = 1.09) by the five-hole probe. In the absence of rotor blades, β increases linearly with C_F with the trend (by definition) intersecting the origin. The annulus swirl is more than twice the disc speed for $C_F > 0.5$. In contrast, the annulus flow is reversed by the bladed rotors and β decreases monotonically from unity; the rate of decline is proportional to the degree of reaction. The measurements of swirl ratio were independent of downstream sealing flow rate and seal geometry. Each set of data

was fitted with a linear trendline to determine a functional relationship between β and C_F at mid-span of the annulus.

Using the linear relationships determined in Figure 12, the effectiveness data in Figure 10 were transposed from C_F to β; the results are shown in Figure 13. All three configurations demonstrate very similar effectiveness for a given annulus swirl ratio, despite the significant differences in the method used to create the fluid-dynamic conditions in the annulus. This result is significant as it indicates the annulus swirl ratio can be used as a parameter to correlate ingress into the wheel-space through the rim seal. The collapse of the data between the two bladed cases is especially convincing, despite the small difference in the maximum effectiveness at a peak swirl ratio $\beta_p \approx 0.3$. Note that similar results were drawn when resolving swirl at other radial positions for $r/b < 1.08$. The data for the bladeless rotor overlaps with the bladed cases for $\beta < 0.7$ and extends the trend beyond $\beta > 2$. The collapse of the data is not as clear as that for the bladed rotors, probably because β varies with radius for this case and the ingested flow is not represented appropriately by the mid-span measurements.

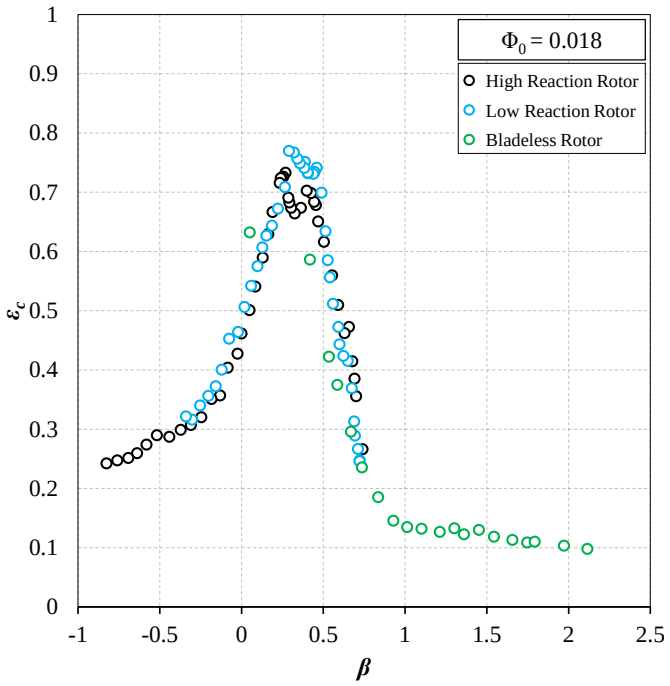

Figure 13: Variation of effectiveness ε_c at r/b = 0.958 against mid-span annulus swirl ratio β for the axial-clearance seal. (Green: Bladeless rotor, Black: High reaction rotor, Blue: Low reaction rotor) Φ_0 = 0.018.

The datasets in Figure 12 were extracted at mid-span in the turbine annulus, demonstrating a collapse between the three test configurations; a similar conclusion was drawn when resolving data at other radial positions. Mid-span was chosen as a convenient location which provided the closest agreement between datasets across the range of flow conditions and seals tested. It is possible in more realistic turbine configurations with non-prismatic twisted blades and higher aspect ratio profiles that mid-span may not be the most appropriate position to use. This however is beyond the scope of the current work.

4.2 Interpretation using turbulent transport model

In this section the experimental measurements are interpreted in terms of the turbulent transport model proposed by Savov and Atkins [7]. Based on the data presented in Figure 13, the model has been adjusted using an effective turbulent mixing length that depends on the difference in swirl ratio between the annulus and that in the rim seal.

Savov and Atkins fitted concentration effectiveness (ε_c) against non-dimensional purge, Φ_0:

$$\varepsilon_c = \frac{1}{1 + k\left(\frac{l_m}{L_{med}}\right)(1 - \mathrm{B}\Phi_0)\,\frac{1}{\Phi_0^2}\,\varepsilon_c} \qquad (5)$$

where

$$\mathrm{B} = c\,\frac{\mathrm{DR}\cos(\alpha)}{\mathrm{VF}\ \times\ \mathrm{AR}\ \times C_F} \qquad (6)$$

and L_{med}, VF and AR are the medial length, volume fraction and area ratio of the rim seal. DR is the density ratio between the purge flow and the annulus flow, and k a constant of proportionality ($= 10^{-5}$). l_m is the effective turbulent eddy mixing length that determines the strength of the turbulent diffusion and hence the ingress mass flux. Here c is a constant to account for the reduction of the diffusion (and associated turbulent transport) due to the radial suppression of the GRZ. A fixed c = 9.7 for both the axial-clearance and double-radial seals was used to account for the reduced influence of the GRZ. The reader is referred to [7] for more details of the derivation and definitions. An explicit form of this equation has been derived here:

$$\varepsilon_c = \frac{-\Phi_0^2 + \sqrt{\Phi_0^4 + 4\Phi_0^2\left(\frac{kl_m}{L_{med}}\right)(1 - \mathrm{B}\Phi_0)}}{2\left(\frac{kl_m}{L_{med}}\right)(1 - \mathrm{B}\Phi_0)} \qquad (7)$$

In this model, the ingress mass flux was determined based on Fick's Law for turbulent diffusion. An effective diffusivity, which is proportional to the effective mixing length l_m, is used to subsume all transport mechanisms, including pressure variations in the annulus and effects of shear between the annulus and the seal clearance flows. Figure 13 shows the effectiveness, or the ingress mass flux, correlates with the swirl ratio in the annulus. Therefore, it is assumed that the effective turbulent mixing length is principally a function that depends on the difference in swirl ratio between the annulus and that in the rim seal, the latter equated to β_p: $l_m = l_m (\left| \beta - \beta_p \right|)$. This can be interpreted by considering larger differences in swirl ratio leading to stronger effects of shear; in turn there will be amplified transport and an increased flux of ingress that decreases sealing effectiveness. Note that $0.25 < \beta_p < 0.4$ for both seals, which is at similar magnitude to that expected for turbulent Couette flow through the seal clearance [16].

The correlation is given by an *ad hoc* equation that relates the swirl ratio to the mixing length:

$$l_m/b = A_1 \exp(A_2 \left| \beta - \beta_p \right|^{A_3}) \qquad (8)$$

Here A_1, A_2 and A_3 are empirical parameters. For a given seal (the axial seal or the double seal), the measurements of effectiveness, velocities and purge flow rates are fitted to achieve these empirical parameters. The optimal correlations for the axial seal and the double seal are given in Equations 9 and 10 below, with the values for the constants listed in Table 4:

Axial seal: $l_m/b = 0.13\exp(5.32|\beta - 0.31|^{0.42})$ (9)

Double seal: $l_m/b = 6 \cdot 10^{-10}\exp(24|\beta - 0.25|^{0.14})$ (10)

	c	β_p	A_1	A_2	A_3	σ
Axial Seal	9.7	0.31	0.13	5.32	0.42	0.084
Double Radial Seal		0.25	6×10^{-10}	24.0	0.14	0.044

Table 4: Coefficients for Equations 8-10

Table 5 gives the geometric parameters used for the two seals that feature in this study with reference to [7].

	L_{med}/b	AR	VF^{-1}
Axial Seal	0.029	2.45	1.13
Double Radial Seal	0.048	3.82	1.85

Table 5: Geometric parameters used for fitting

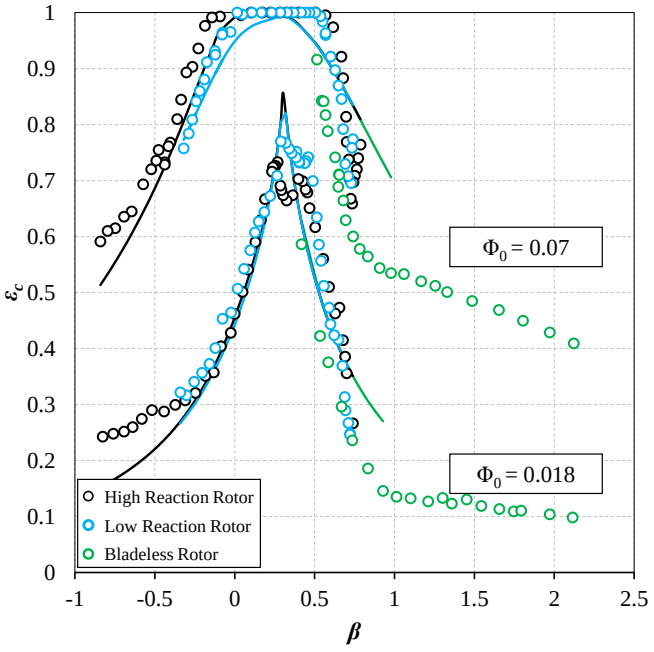

Figure 14: Effectiveness ε_c at r/b = 0.958 against mid-span annulus swirl ratio β for the axial-clearance seal. (Green: Bladeless rotor, Black: High reaction rotor, Blue: Low reaction rotor, symbols represent experimental data and lines theoretical fits) Φ_0 = 0.018 and Φ_0 = 0.07.

Figure 14 presents the agreement between the model and experimental data from Figure 13 for Φ_0 = 0.018. A similar analysis was conducted at Φ_0 = 0.07 with the data and model also shown in Figure 14. The effectiveness has increased at increased Φ_0 with the data for the bladed rotors saturating over the range $0 > \beta > 0.5$ where $\varepsilon_c = 1$; here ingress is prevented and therefore a distinct peak no longer observed. The three sets of data again collapse to a common curve when plotted against the swirl ratio in the annulus.

The model presented here is consistent with the findings of Mirzamoghadam *et al*. [13] and Scobie *et al.* 2013 [14], which indicated a minimum level of ingress at a critical C_F corresponding to $\beta \sim 0.3$; here it is speculated there was a minimum difference in swirl between the annulus and seal clearance. The subsequent increase of ingress after the critical C_F was caused by the increase of the swirl ratio difference. As discussed below, the results are also consistent with Hualca *et al.* [17].

4.3 Pressure asymmetry in the annulus

Figure 15 presents the non-dimensional circumferentially variation in annulus pressure coefficient, $C_{p,a,}$ measured on the stator hub for all three rotor configurations. The data is collected over a vane pitch ($0 < \theta < 1$). The results show that over a range of flow coefficient the influence of the upstream vane is apparent, despite being measured at the downstream stator platform. There is a pressure variation

corresponding to a vane pitch that peaks at a certain C_F depending on the blade design. The reason this can be observed downstream of the blade, and at a significant axial distance from the source, is due to a phenomenon known as wake recovery [18].

Wake recovery is the amplification of the wake-velocity profile in a turbine by processes other than viscous dissipation occurring inside a blade row. The wake from the upstream vane may be characterised by the peak-to-trough variation of non-dimensional pressure coefficient, $\Delta C_{p,a}$. Dispersion of $\Delta C_{p,a}$ will be reduced through the downstream blade row: the rate of decay of the vane wake will be diminished by the presence of the blade. The stronger the flow acceleration (higher C_F or higher the rotor reaction) through the blade passage, the slower the wake decay. As a consequence, $\Delta C_{p,a}$ for the higher reaction blade is greater, *i.e.* the lower reaction requires a larger flow coefficient to create the same $\Delta C_{p,a}$. The wake for the bladeless rotor has almost decayed completely at the downstream stator platform. This is primarily an inviscid flow phenomenon. The opposite will occur for flow in a compressor, i.e. wake recovery is enhanced by the presence of a downstream blade row.

Critically, the bladeless case exhibits the largest amount of ingress of three configurations (see Figure 10), despite the least measured circumferential pressure variation. This direct evidence contradicts the traditional thinking that ingress is driven by such pressure variations.

The results presented here are consistent with the findings of Hualca *et al.* [17]; they showed that axially displacing the upstream vane significantly increased $\Delta C_{p,a}$ measured on the upstream stator platform, yet the ingress into the upstream wheel-space remained unchanged. The annulus swirl for the two axial vane positions were consistent, a result supported by the findings of this study.

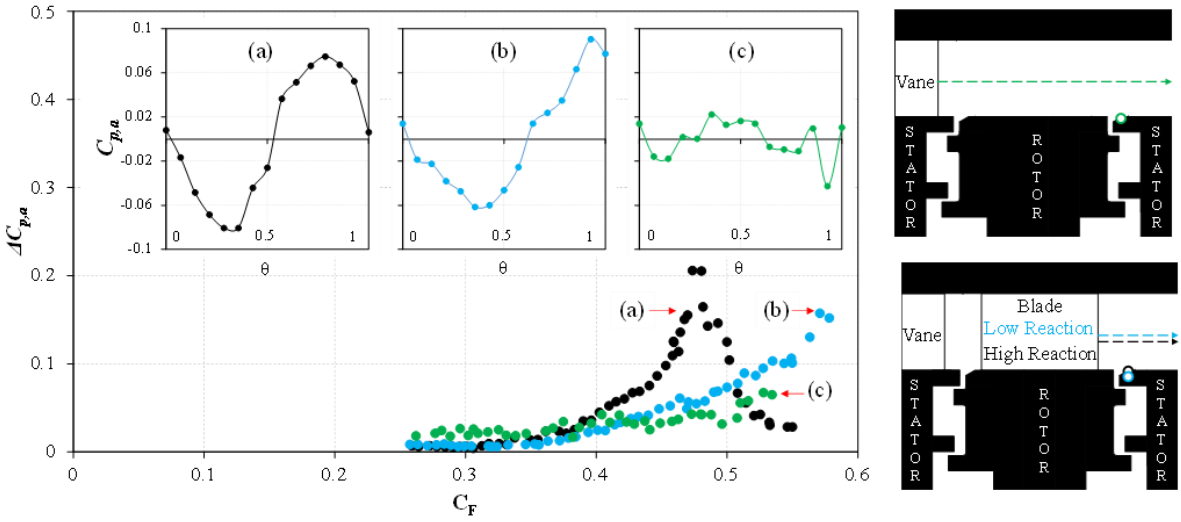

Figure 15: Wake recovery effect of the upstream vane

4.4 Double radial-clearance seal

Figure 16 shows the variation of effectiveness against annulus swirl for the double radial-clearance seal, tested using the same sealing flow rate (Φ_0 = 0.018) as the axial-clearance seal shown in Figure 13 and Figure 14. Results for the turbulent-transport model with l_m given by Equation 7 are also shown. The double seal offers improved sealing performance for comparable flow conditions in the annulus. For the axial-clearance seal, $\varepsilon_c \approx 0.76$ at $\beta_p = 0.31$; at this swirl ratio the double-clearance configuration is virtually sealed, *i.e.* $\varepsilon_c \approx 1$. No effectiveness measurements are presented here at lower radius through the inner rim seal. The inner wheel-space would be fully sealed over a wide range of β at Φ_0 = 0.018 [12].

Results at a larger sealing flow rate (Φ_0 = 0.034) are shown in Figure 17. The outer wheel-space is sealed over a wider range of annulus swirl ($0 < \beta < 0.5$) as the increased purge pressurises the cavity. The collapse of data between the three rotor configurations when ingress is present is again good, demonstrating a consistent influence of annulus swirl ratio. Comparison of the standard deviations for the fits given in Table 4 confirm

that agreement between experiment and theory is generally better for the double radial seal compared to the axial.

The suppression of the GRZ with increasing purge is illustrated in Figure 2, with it eventually ejected from the rim seal; the associated turbulent transport must diminish and eventually cease with increasing purge. This effect is modelled in Equations 5 and 6 but cannot be explicitly decoupled from the effect of difference in swirl ratio.

Consider further the case with no blades in the annulus – bladeless rotor. For both seal geometries, and all sealing flow rates tested, there is a distinct inflection in the influence of swirl at $\beta = 1$. This is attributed to a transition where the rotor disc switches from accelerating the annulus flow at the hub, to acting against the direction of the flow. For this reason, the bladeless rotor data is only fitted using the turbulent transport model for $\beta < 1$.

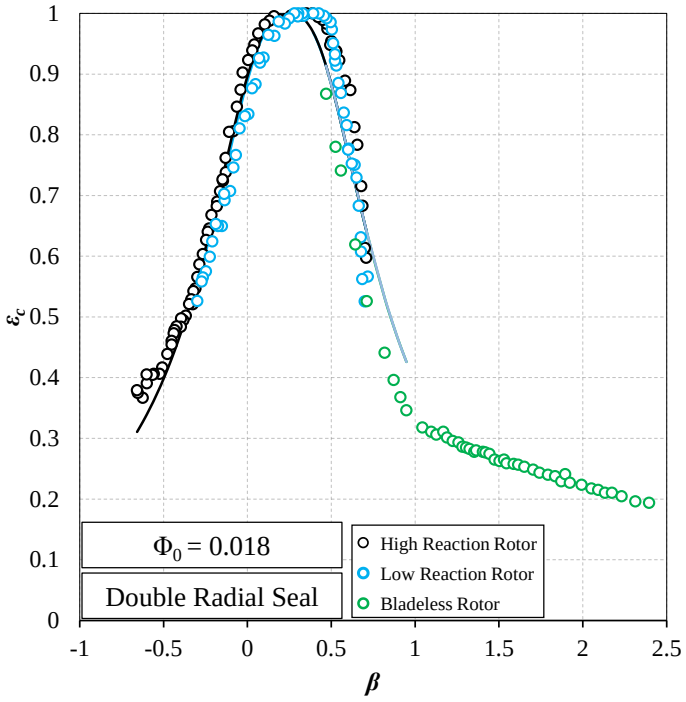

Figure 16: Effectiveness ε_c at $r/b = 0.958$ against mid-span annulus swirl ratio β for the double radial-clearance seal. (Green: Bladeless rotor, Black: High

reaction rotor, Blue: Low reaction rotor, symbols represent experimental data and lines theoretical fits) Φ_0 = 0.018.

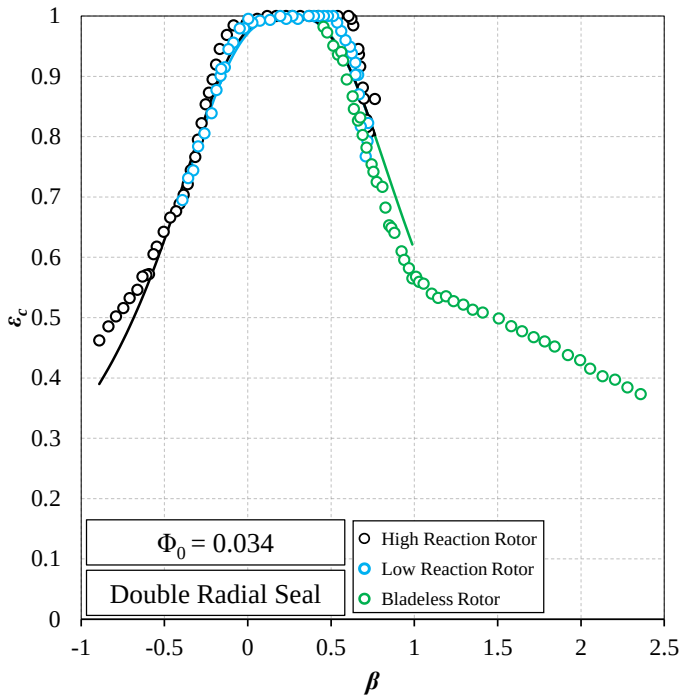

Figure 17: Effectiveness ε_c at r/b = 0.958 against mid-span annulus swirl ratio β for the double radial-clearance seal. (Green: Bladeless rotor, Black: High reaction rotor, Blue: Low reaction rotor, symbols represent experimental data and lines theoretical fits) Φ_0 = 0.034.

4.5 Application to practical engine design

As discussed in Section 2, low-order models are often used to characterise experimental data from turbine rigs operating at benign conditions and low Reynolds number. Engineers require predictive methods that scale reliably to engine conditions to support practical industrial design. This paper has shown that ingress can be correlated with the swirl ratio in the annulus, a parameter that can be determined with some confidence as it can be computed from a knowledge of the blade and vane

geometries. The designer can also reliably calculate the influence of higher Reynolds and Mach numbers on swirl.

Following the work of Savov and Atkins [7], this paper has provided further confidence in modelling an effective turbulent eddy mixing length that determines the strength of the turbulent diffusion and hence the ingress mass flux. There are obvious limitations of the model; these include a single empirical constant appropriate over a limited range of interest appropriate for industrial design. Further, the model (as with all low-order models) requires information from experiments to establish empirical parameters that are geometry-dependent. Scaling is also restricted by the limits of dimensional similitude.

5 CONCLUSIONS

A turbine rig operating at a low Reynolds number has been used to measure the ingress through rim seals downstream of the rotor, with concentration effectiveness determined using a CO_2 tracer gas in the purge. Swirl was measured in the wheel-space and in the annulus near the rim seals using a five-hole aerodynamic probe. Three interchangeable modular bliscs were used: two with turned rotor blades but of different degrees of reaction, and one with no blades (i.e. a rotating ring). The annulus swirl above the rim seal was controlled by varying the flow coefficient and by using the different rotors. The experiments thus correlated the rim-seal effectiveness in a manner where C_F and β are decoupled.

The experiments reveal a general collapse of data and a similar effectiveness for a given annulus swirl ratio, despite the significant differences in the method used to create the fluid-dynamic conditions in the annulus. This result is significant as it indicates the annulus swirl ratio can be used as a parameter to correlate ingress through the rim seal.

The investigation presents a new interpretation of the driving mechanism for ingress. The analysis was supported by extending a low-order model based on turbulent transport, using an effective mixing length that depended principally on the difference in swirl between the annulus and rim-seal clearance; larger differences in swirl were associated with more intense levels of shear, and in turn amplified diffusion and increased flux of ingress.

The results are of practical interest to the engine designer providing improved predictive capability for thermal management, especially in terms of scaling rig data to engine conditions.

ACKNOWLEDGEMENTS

The authors would like to acknowledge Yan Sheng Li from Siemens Energy, Lincoln for his help in explaining the pressure data, especially in relation to Figure 15.

DATA ACCESS

Due to confidentiality agreements with research collaborators, supporting data can only be made available to bona fide researchers subject to a nondisclosure agreement. Details of how to request access are available at the University of Bath data archive (http://dx.doi.org/10.15125/BATH-00116).

FUNDING DATA

Engineering and Physical Sciences Research Council (EP/J014826/1).

NOMENCLATURE

$A_{1,2,3}$ *constants*

AR *area ratio (= $s_p/s_{c,ax}$)*

a *speed of sound (m/s)*

B *turbulent mixing switch-off parameter*

b *radius of seal (m)*

c *concentration of tracer gas (%); constant*

C *absolute velocity (m/s)*

C_F *flow coefficient ($W/\Omega b$)*

$C_{p,a}$ *pressure coefficient in annulus (= $(p_a-\bar{p}_a)/\frac{1}{2}\rho\Omega^2 b^2$)*

$\Delta C_{p,a}$ *peak-to-trough variation of $C_{p,a}$*

$C_{w,0}$ *nondimensional sealing flow rate (= $\dot{m}/\mu b$)*

DR *density ratio (ρ_a/ρ_0)*

G_c *seal-clearance ratio (= $s_{c,ax}/b$)*

GRZ *gap recirculation zone*

HR *high reaction*

h *height of annulus (m)*

k *turbulent velocity scaling factor*

L_{med} *medial length scale (m)*

l_m *effective turbulent eddy mixing length (m)*

LR *low reaction*

$\dot{m}$ *mass flow rate (kg/s)*

M *Mach number*

r *radius (m)*

Re_w *axial Reynolds number in annulus based on radius (= $\rho W b/\mu$)*

Re_ϕ *rotational Reynolds number (= $\rho\Omega b^2/\mu$)*

s_c *seal clearance (m)*

s_p *clearance at rim seal throat exit (m)*

S *axial clearance between rotor and stator (m)*

U *bulk mean radial seal velocity (= $\dot{m}_0/2\pi\rho b s_{c,ax}$)*

V *relative velocity (m/s)*

VF *seal volume fraction (= s_p/L_{med})*

W *mean axial velocity in annulus (m/s)*

z *axial coordinate (m)*

α_2 *vane exit angle (deg)*

α_3 *blade exit angle (deg)*

β *swirl ratio (= $V_\phi/(\Omega r)$)*

β_2 *relative blade inlet angle (deg)*

β_3 *relative blade exit angle (deg)*

ε_c *concentration effectiveness*

Λ *degree of reaction*

μ *dynamic viscosity (kg/ms)*

ρ *density (kg/m^3)*

σ *standard deviation*

Φ_0 *non-dimensional sealing parameter (= $U/\Omega b$)*

ψ *blade loading coefficient*

Ω *angular speed of rotating disc (rad/s)*

Subscripts

a *annulus*

ax *axial*

c *concentration*

p	*peak*
rad	*radial*
s	*stator surface*
0	*sealing flow*
2	*location upstream of blades*
3	*location downstream of blades*
ϕ	*tangential direction*

References

[1] Chew, J. W., Gao, F., and Palermo, D. M., 2019, "Flow Mechanisms in Axial Turbine Rim Sealing," Proc. Inst. Mech. Eng. Part C J. Mech. Eng. Sci., 233(23–24), pp. 7637–7657.

[2] Owen, J. M., 2011, "Prediction of Ingestion through Turbine Rim Seals. Part I: Rotationally Induced Ingress," ASME J. Turbomach., 133(3), 031005.

[3] Owen, J. M., 2011, "Prediction of Ingestion through Turbine Rim Seals. Part II: Externally Induced and Combined Ingress," ASME J. Turbomach., 133(3), 031006.

[4] Johnson, B. V., Wang, C. Z., and Roy, R., 2008, "A rim seal orifice model with two cds and effects of swirl in seals," ASME Paper No. GT2008-50650.

[5] Scobie, J. A., Sangan, C. M., Owen, J. M., and Lock, G. D., 2016, "Review of Ingress in Gas Turbines," ASME J. Eng. Gas Turb. Power, 138(12), p.120801.

[6] Graber, D., Daniels, W., and Johnson, B., 1987, "Disk pumping test". Air Force Wright Aeronautical Laboratories Technical Report (AFWAL-TR-87-2050), September.

[7] Savov, S.S. and Atkins, N.R., 2017, “A Rim Seal Ingress Model Based on Turbulent Transport,” ASME Paper No. GT2017- 63531.

[8] B. S. Massey., 1989, “Mechanics of Fluids,” Oxford University Press, Sixth Edition.

[9] Ko, S. H. and Rhode, D. L., 1992, “Thermal details in a rotor–stator cavity at engine conditions with a mainstream,” ASME J. Turbomach., 114(2), pp. 446–453.

[10] Rabs, M., Benra, F.-K., Dohmen, H.J. and Schneider, O., 2009, “Investigation of flow instabilities near the rim cavity of a 1.5 stage gas turbine,” ASME Paper No. GT2009-59965.

[11] Beard, P. F., Gao, F., Chana, K. S. and Chew, J. W., 2017, “Unsteady Flow Phenomena in Turbine Rim Seals,” ASME J. Eng. Gas Turb. Power, 139(3), p. 032501.

[12] Graikos, D., Carnevale, M., Sangan, C. M., Lock, G. D., and Scobie, J. A., 2021, “Influence of Flow Coefficient on Ingress Through Turbine Rim Seals,” ASME. J. Eng. Gas Turbines Power, 143(11), p.111010.

[13] Mirzamoghadam, A. V., Heitland, G., and Molla-Hosseini, K. 2014. “The Effect of Annulus Performance Parameters on Rotor-Stator Cavity Sealing Flow,” ASME. J. Thermal Sci. Eng. Appl., 6(3), p.031013.

[14] Scobie, J. A., Sangan, C. M., O. J., Owen, J. M., Wilson, M., and Lock, G. D., 2014, “Experimental measurements of hot gas ingestion through turbine rim seals at off-design conditions,” Proc. IMechE Part A: J. Power and Energy, 228 (5), p. 491-507.

[15] Patinios, M., Scobie, J. A., Sangan, C. M., Owen, J. M. and Lock, G. D., 2017, "Measurements and Modelling of Ingress in a New 1.5-Stage Turbine Research Facility," ASME J. Eng. Gas Turb. Power, 139, p.012603.

[16] Palermo, D. M., Gao, F., Chew, J. W., and Beard, P. F. 2019, "Effect of annulus flow conditions on turbine rim seal ingestion," ASME Paper GT2019-90489

[17] Hualca, F. P., Horwood, J. T. M., Sangan, C. M., Lock, G. D. and Scobie, J. A., 2020, "The Effect of Vanes and Blades on Ingress in Gas Turbines," ASME J. Eng. Gas Turb. Power, 142 (2), p.021020.

[18] Smith, L. H., Jr., 1966, ''Wake Dispersion in Turbomachines,'' J. Basic Eng., pp. 688–690.